AN EFFECTIVE METHOD TO SUPPRESS NUMERICAL DISPERSION IN 3D ELASTIC MODELING USING A HIGH-ORDER PADÉ APPROXIMATION

YANJIE ZHOU[1], XUEYUAN HUANG[1], XIJUN HE[1] and YONGCHANG ZHENG[2]

[1] *Department of Mathematics, School of Mathematics and Statistics, Beijing Technology and Business University (BTBU), Beijing 100048, P.R. China. zhouyanjie9@163.com*
[2] *Department of Liver Surgery, Peking Union Medical College Hospital, Chinese Academy of Medical Sciences, Beijing 100730, P.R. China.*

ABSTRACT

Zhou, Y.J., Huang, X.Y., He, X.J. and Zheng, Y.C., 2020. An effective method to suppress numerical dispersion in 3D elastic modeling using a high-order Padé approximation. *Journal of Seismic Exploration*, 29: 425-454.

We proposed a numerical method for solving seismic wave equations called the fourth-order Padé approximation method (PAM). This work was an extension of the 2D PAM to the 3D case. We used the PAM for time discretization to obtain an implicit scheme, in which the time difference operator has a rational function form. To avoid solving large linear systems with a block tridiagonal coefficient matrix, we proposed an algorithm to transform the implicit scheme into an explicit method. For the spatial discretization, we adapted the nearly analytic discrete (NAD) operator, which uses a linear combination of wavefield displacements and their gradients to discretize higher-order spatial derivatives. In addition, for the fourth- and fifth-order mixed partial differential terms, we used operator splitting to reduce the order of the differential operators in the scheme and decrease the calculation time. The proposed scheme had higher precision with eighth-order accuracy in space, lower dispersion, and higher computational efficiency than the other Padé approximation-based approaches, which were fourth-order compact finite difference schemes that required solving a large tridiagonal system at each time step. The stability condition, relative error, and dispersion relation of the 3D PAM were analyzed. Comparisons of the theoretical and numerical results of the proposed method, the 3D Lax-Wendroff correction (LWC) method, and the staggered grid (SG) finite difference method demonstrated the superiority of the PAM for solving 3D seismic wave equations and its advantages of lower dispersion and higher computational efficiency. The results indicated that the 3D high-order PAM was an efficient and accurate forward modeling tool for solving large-scale wave propagation problems related to reverse time migration or full-waveform inversion.

INTRODUCTION

Numerically solving wave equations has become a powerful tool in seismological research. An accurate and efficient method to generate synthetic seismograms is a core requirement to determine the Earth's structure. Many numerical methods were proposed and have been widely used, such as the finite-difference method (e.g., Virieux, 1984, 1986; Alterman and Karal, 1968; Dablain, 1986; Blanch and Robertsson, 2010; Carcione and Helle, 1999; Moczo et al., 2002), the finite-element method (e.g., Eriksson and Johnson, 1991; Yang, 2002), the pseudo-spectral method (e.g., Kosloff, 1984; Huang, 1992; Carcione, 2014), the spectral element method (e.g., Seriani, 1992; Komatitsch and Vilotte, 1998), the reflective method (Booth and Crampin, 1983a, 1983b; Chen, 1993), the boundary integral equation-discrete wavenumber method (e.g., Bouchon, 1996; Zhou and Chen, 2008), and the discontinuous Galerkin (DG) method (e.g., Käser and Dumbser, 2006; He et al., 2014, 2015; Yang et al., 2016). Each method has its advantages and drawbacks. Numerous studies have investigated the theoretical properties of these methods (e.g., Yang et al., 2002, 2003). Finite-difference methods are most widely used due to their simplicity in implementation and high efficiency. However, conventional finite-difference methods suffer from strong numerical dispersion when the number of grid points per wavelength is insufficient, or the media have complex structures (Fei and Larner, 1995; Yang et al., 2010). In order to avoid numerical dispersion, a simple approach is to increase the number of spatial sampling grid points per wavelength or increase the accuracy of the numerical scheme. However, this method results in a rapid increase in computational and storage costs (Takeuchi and Geller, 2000; Liu and Sen, 2010). Hence, further improvements in the numerical methods are essential.

The Padé approximation has attracted much attention in recent years (Kosloff et al., 2010; Das et al., 2014; Zhang et al., 2015; Tong et al., 2013; Abdulkadir, 2015). Kosloff et al., (2010) compared the Padé method with the use of recursive spatial derivative operators. Das et al. (2014) combined the alternating direction implicit (ADI) technique with the Padé approximation and non-compact stages and developed the interlinked Padé approximation-based ADI scheme (IPD-ADI). Those hybrid schemes are only fourth-order compact finite difference schemes and require solving a large tridiagonal system at each time step (the scheme in the decoupled form uses intermediate values). Abdulkadir (2015) compared the dispersion properties of three higher-order finite difference schemes and showed that the non-compact Padé-based method had a relatively lower dispersion error than the compact Padé and higher-order compact methods. Salcedo et al. (2017) applied the complex Padé Fourier finite difference method to seismic migration.

The nearly analytic discrete (NAD) method has attracted the attention of researchers working on seismic wave propagation since it was first introduced by Yang et al. (2002, 2003). Subsequently, the method was widely used in forward modeling methods for solving wave equations (Yang et al., 2014; Ma et al., 2014, 2015; Huang et al., 2016). NAD is an

effective numerical method that suppresses numerical dispersion and provides high spatial accuracy. Zhou et al. (2015) developed the Padé approximation method (PAM) and used it for solving large-scale problems in 2D forward modeling due to its low numerical dispersion and high computational efficiency. Compared with the Lax-Wendroff correction (LWC) method (Dablain, 1986) and the staggered grid (SG) finite-difference method (Virieux, 1984, 1986; Graves, 1996), the 2D PAM method provides better suppression of numerical dispersion with a relatively coarse grid, thereby saving computational time and memory. However, the PAM method has not been applied to the 3D case to date since the extension to 3D is more than straightforward. The primary objective of this study is to develop a 3D high-order finite difference method based on the PAM to suppress the numerical dispersion for modeling wave propagation in both isotropic and anisotropic media using large grid steps. We first transform the wave equations into a system of semi-discrete ordinary differential equations according to the Padé approximation scheme. Subsequently, the eight-order stereo-modeling method (SMM) operators and operator-splitting method are used for spatial discretization. The eighth-order LWC and SG methods are used for comparison in a 3D framework. We analyze the numerical dispersion and stability of the 3D PAM and compare the waveforms computed by the 3D PAM with the analytical solutions. Finally, we use the 3D PAM to perform wave simulations of 3D multi-layer acoustic layers in isotropic and transversely isotropic elastic media.

THE PADÉ APPROXIMATION METHOD

We first describe the discrete scheme in this section to demonstrate the application of PAM in a 3D framework. The strong form of the 3D seismic wave equation of motion has the following form:

$$\rho \frac{\partial^2 u}{\partial t^2} = \nabla \cdot \left(\mathbf{c} : \nabla u \right) + f(t)\delta(x - x_s, y - y_s, z - z_s), \tag{1}$$

where the displacement vector is $u(\mathbf{x},t) = (u_1, u_2, u_3)$, with u_1, u_2 and u_3 respectively denoting the x-, y-, and z-components; $\mathbf{c}$ is the elastic tensor; $\nabla = \left(\dfrac{\partial}{\partial x}, \dfrac{\partial}{\partial y}, \dfrac{\partial}{\partial z} \right)^T$; ρ is the density and ":" is the contraction symbol. $f(t)$ is the force source, $\delta(x - x_s, y - y_s, z - z_s)$ is the Dirac function, (x_s, y_s, z_s) is the location of the seismic source. The 3D acoustic equation is expressed as:

$$\frac{\partial^2 u}{\partial t^2} = c_0^2 \left(\frac{\partial^2 u}{\partial x^2} + \frac{\partial^2 u}{\partial y^2} + \frac{\partial^2 u}{\partial z^2} \right) + f(t)\delta(x - x_s, y - y_s, z - z_s). \tag{2}$$

Eq. (2) can be rewritten as

$$\frac{\partial^2 u}{\partial t^2} = D \cdot u + f , \tag{3}$$

where $D = c_0{}^2 (\frac{\partial^2}{\partial x^2} + \frac{\partial^2}{\partial y^2} + \frac{\partial^2}{\partial z^2})$, in which c_0 is the wave velocity.

Let $U = (u, \frac{\partial u}{\partial x}, \frac{\partial u}{\partial y}, \frac{\partial u}{\partial z})^T$, according to eq. (3), we obtain：

$$\frac{\partial^2 U}{\partial t^2} = \overline{L}U + F , \tag{4}$$

while $\overline{L}$ and F are respectively defined as：

$$\overline{L} = \begin{pmatrix} D & 0 & 0 & 0 \\ 0 & D & 0 & 0 \\ 0 & 0 & D & 0 \\ 0 & 0 & 0 & D \end{pmatrix}, \quad F = (f, 0, 0, 0)^T . \tag{5}$$

In the time-marching scheme of eq. (3), similar to the discretization of the 2D acoustic wave equations, we use the fourth-order Padé approximation to obtain the following scheme:

$$\frac{1}{(\Delta t)^2} \frac{\delta_t^2}{1 + \frac{1}{12}\delta_t^2} U_{i,j,k}^n = \frac{\partial^2 U_{i,j,k}^n}{\partial t^2} + O((\Delta t)^4) \tag{6}$$

where $U_{i,j,k}^n = U(x_i, y_j, z_k, t_n)$, $\delta_t^2 U_{i,j,k}^n = U_{i,j,k}^{n+1} - 2U_{i,j,k}^n + U_{i,j,k}^{n-1}$, and Δt is the time increment. Thus, the time-marching equation that ignores the fourth-order error term is expressed as:

$$(I - \frac{(\Delta t)^2}{12}\overline{L})U_{i,j,k}^{n+1} = (\frac{5(\Delta t)^2}{6}\overline{L} + 2I)U_{i,j,k}^n + (\frac{(\Delta t)^2}{12}\overline{L} - I)U_{i,j,k}^{n-1} + ((\Delta t)^2 + \frac{(\Delta t)^2}{12}\delta_t^2)F , \tag{7}$$

where I is an identity operator.

It is evident that algorithm (7) is explicit. We convert the explicit algorithm into an implicit algorithm to avoid solving a system of linear equations at each time step. We assume that the operator $\overline{L}$ satisfies

$\left\|\dfrac{(\Delta t)^2}{12}\overline{L}\right\| \leq 1$, and we use the truncated Taylor expansion. The 3D PAM is expressed as follows (Wang and Zhou, 2014, 2015), and we obtain an explicit scheme of the time-marching equation of the 3D acoustic wave equation :

$$U_{i,j,k}^{n+1} = (V_{i,j,k}^n + W_{i,j,k}^{n-1}) + (\frac{(\Delta t)^2}{12}\overline{L})(V_{i,j,k}^n + W_{i,j,k}^{n-1}) + (\frac{(\Delta t)^2}{12}\overline{L})[(\frac{(\Delta t)^2}{12}\overline{L})(V_{i,j,k}^n + W_{i,j,k}^{n-1})] + \overline{F} \quad (8)$$

where

$$V_{i,j,k}^n = (\frac{5(\Delta t)^2}{6}\overline{L} + 2I)U_{i,j,k}^n, \qquad W_{i,j,k}^{n-1} = (\frac{(\Delta t)^2}{12}\overline{L} - I)U_{i,j,k}^{n-1},$$

$$\overline{F} = (\frac{1}{\rho}\Delta t^2(f(t) + \frac{1}{12}(f(t+\Delta t) - 2f(t) + f(t-\Delta t)),0,0)^T.$$

In the following part, we introduce the scheme for the elastic case. In a 3D heterogeneous elastic medium, the seismic wave equation is defined as：

$$\rho\frac{\partial^2 u}{\partial t^2} = Lu + F \qquad , \tag{9}$$

where $u = (u_1, u_2, u_3), F = (f_1, f_2, f_3)$. L is defined by:

$$L = \begin{pmatrix} (\lambda+2\mu)\dfrac{\partial^2}{\partial x^2} + \mu\dfrac{\partial^2}{\partial y^2} + \mu\dfrac{\partial^2}{\partial z^2} & (\lambda+\mu)\dfrac{\partial^2}{\partial x\partial y} & (\lambda+\mu)\dfrac{\partial^2}{\partial x\partial z} \\ (\lambda+\mu)\dfrac{\partial^2}{\partial x\partial y} & (\lambda+2\mu)\dfrac{\partial^2}{\partial y^2} + \mu\dfrac{\partial^2}{\partial x^2} + \mu\dfrac{\partial^2}{\partial z^2} & (\lambda+\mu)\dfrac{\partial^2}{\partial y\partial z} \\ (\lambda+\mu)\dfrac{\partial^2}{\partial x\partial z} & (\lambda+\mu)\dfrac{\partial^2}{\partial y\partial z} & (\lambda+2\mu)\dfrac{\partial^2}{\partial z^2} + \mu\dfrac{\partial^2}{\partial x^2} + \mu\dfrac{\partial^2}{\partial y^2} \end{pmatrix}$$

$$\tag{10}$$

let $\widetilde{U} = (u, \dfrac{\partial u}{\partial x}, \dfrac{\partial u}{\partial y}, \dfrac{\partial u}{\partial z})^T$, then:

$$\frac{\partial^2 \widetilde{U}}{\partial t^2} = \widetilde{L}\widetilde{U} + \widetilde{F} \quad , \tag{11}$$

where

$$\tilde{L}=\begin{pmatrix} L & & & \\ & L & & \\ & & L & \\ & & & L \end{pmatrix} \qquad \tilde{F}=\begin{pmatrix} F \\ 0 \\ 0 \\ 0 \end{pmatrix} \qquad .$$

When the operator $\tilde{L}$ satisfies

$$\left\| \frac{(\Delta t)^2}{12} \tilde{L} \right\| \le 1,$$

we can obtain the explicit PAM algorithm for the 3D elastic wave equation:

$$\tilde{U}_{i,j,k}^{n+1} = (V_{i,j,k}^{n} + W_{i,j,k}^{n-1}) + (\frac{(\Delta t)^2}{12}\tilde{L})(V_{i,j,k}^{n} + W_{i,j,k}^{n-1}) + (\frac{(\Delta t)^2}{12}\tilde{L})[(\frac{(\Delta t)^2}{12}\tilde{L})(V_{i,j,k}^{n} + W_{i,j,k}^{n-1})] + \tilde{F} \quad (12)$$

where

$$V_{i,j,k}^{n} = (\frac{5(\Delta t)^2}{6}\tilde{L} + 2I)\tilde{U}_{i,j,k}^{n}, \qquad W_{i,j,k}^{n-1} = (\frac{(\Delta t)^2}{12}\tilde{L} - I)\tilde{U}_{i,j,k}^{n-1}$$

$$\tilde{F} = (\frac{1}{\rho}\Delta t^2(f(t) + \frac{1}{12}(f(t+\Delta t) - 2f(t) + f(t-\Delta t)), 0, 0)^T \qquad (13)$$

It seems that the PAM discretization schemes for the 3D elastic and acoustic wave equations are similar with the 2D case. However, the spatial operator for the elastic wave equations is much more complex. Therefore, as for the approximation of the high-order spatial derivatives, split-step algorithm has much more obvious computational advantages by using the SMM discrete operators twice. There are three steps to compute $\tilde{U}_{i,j,k}^{n+1}$:

1. Compute $V_{i,j,k}^{n}$ and $W_{i,j,k}^{n-1}$ according to eq. (10) using the SMM discrete operators in (A-1) − (A-5);
2. Compute $\tilde{L}(V_{i,j,k}^{n} + W_{i,j,k}^{n-1}) = R_{i,j,k}^{n}$ using the same spatial discrete operators in the first step;
3. Using the results of the second step and applying the same computational formulae to compute $\tilde{L}R_{i,j,k}^{n}$. Then finish the computation $\tilde{U}_{i,j,k}^{n+1} = (V_{i,j,k}^{n} + W_{i,j,k}^{n-1}) + \frac{(\Delta t)^2}{12}R_{i,j,k}^{n} + (\frac{(\Delta t)^2}{12})^2\tilde{L}R_{i,j,k}^{n}$ using eq. (12).

Note that the fourth-term $\tilde{F}$ on the right-hand side of eq. (13) can be easily computed because of the known analytic source function $f(t)$.

ERROR ANALYSIS

Theoretical analysis

Using the Taylor series expansion, we can obtain the errors of the high-order spatial derivations $(\partial^{k+l+m} U / \partial x^k \partial y^l \partial z^m)_{i,j}^n$ $(2 \le k + m + l \le 3)$ using the SMM operator (Yang and Wang, 2010) $O(\Delta x^8 + \Delta y^8 + \Delta z^8)$. In contrast, the temporal error caused by the discretization of the temporal partial derivative is $O(\Delta t^4)$. Therefore, the error introduced by the PAM is $O(\Delta t^4 + \Delta x^8 + \Delta y^8 + \Delta z^8)$. In other words, the proposed 3D PAM has eighth-order accuracy in space and fourth-order accuracy in time.

Numerical error analysis

To illustrate the accuracy of PAM, we compare the numerical errors of the 3D PAM with other traditional methods (the eighth-order LWC and the SG methods) in the framework of solving the 3D acoustic wave equations. Consider the following 3D initial value problem：

$$
\begin{cases}
\dfrac{\partial^2 u}{\partial t^2} = c^2 \left(\dfrac{\partial^2 u}{\partial x^2} + \dfrac{\partial^2 u}{\partial y^2} + \dfrac{\partial^2 u}{\partial z^2} \right) \\[2mm]
u(0,x,y,z) = \cos\left[-\dfrac{2\pi f_0}{c}(l_0 \cdot x + m_0 \cdot y + n_0 \cdot z) \right] \\[2mm]
\dfrac{\partial u(0,x,y,z)}{\partial t} = -2\pi f_0 \sin[-\dfrac{2\pi f_0}{c}(l_0 \cdot x + m_0 \cdot y + n_0 \cdot z)],
\end{cases}
\quad , \quad (14)
$$

where f_0 denotes the frequency, c is the wave velocity, and the vector (l_0, m_0, n_0) is the direction of the incident acoustic wave at time $t = 0$ s. Here the vector is $(l_0, m_0, n_0) = (1/\sqrt{3}, 1/\sqrt{3}, 1/\sqrt{3})$ in the experiment.

The analytical solution of the initial value problem (14) is:

$$
u(t,x,y,z) = \cos[2\pi f_0(t - l_0 \cdot x / c - m_0 \cdot y / c - n_0 \cdot z / c)].
\quad (15)
$$

In the numerical experiment, the relative error (E_r) of the 3D case is defined as follows (Konddoh et al., 1994):

$$E_r(\%) = \left\{ \frac{\sum\limits_{i=1}^{N}\sum\limits_{j=1}^{N}\sum\limits_{k=1}^{N}[u_{i,j,k}^n - u(t_n,x_i,y_j,z_k)]^2}{\sum\limits_{i=1}^{N}\sum\limits_{j=1}^{N}\sum\limits_{k=1}^{N}[u(t_n,x_i,y_j,z_k)]^2} \right\}^{\frac{1}{2}} \times 100 \qquad , \qquad (16)$$

where $u_{i,j,k}^n$ is the numerical solution and $u(t_n,x_i,y_j,z_k)$ is the analytical solution on the discrete grid points of the initial value problem.

The number of grid points is $N_x = N_y = N_z = 251$, the peak frequency $f_0 = 25$ Hz, the acoustic velocity $c = 4000$ m/s, the grid interval $\Delta x = \Delta y = \Delta z = 30$ m, and the time step $\Delta t = 0.0005$ s. Fig. 1 shows the E_r changing over time for different spatial and temporal increments on a semi-log scale; the three lines of E_r correspond to the PAM, the eighth-order LWC method, and the eighth-order SG method. Fig. 1 demonstrates that the PAM has the smallest numerical error.
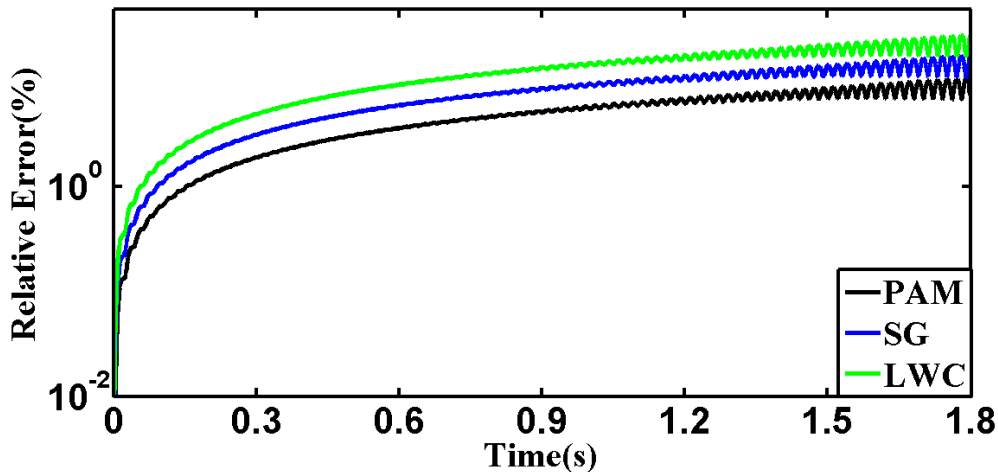

Fig. 1. The relative errors (E_r) (%) of the PAM, the eighth-order LWC method, and the eighth-order SG method [eq. (18)] at the semi-logarithm scale for the 3D initial problem [eq. (15)].

STABILITY CONDITIONS

It is well known that, when numerically solving wave equations, the temporal increment, the spatial increment, and the wave velocity must satisfy a particular relationship to ensure the stability of the numerical calculation. We use Fourier analyses (Richtmyer and Morton, 1994; Guan and Lu, 2006) and follow the analysis methods used in previous studies (e.g., Vichnevetsky, 1979; Dablain, 1986; Yang et al., 2010) to obtain the stability criterion of the PAM for the 3D case. The details of deriving the stability condition of the 3D PAM are discussed in Appendix B; here, we describe the stability condition as follows:

$$\alpha = \frac{c_0 \Delta t}{h} \le \alpha_{\max} \le 0.513 \quad \text{or} \quad \Delta t = \frac{\alpha h}{c_0} \le \frac{\alpha_{\max} h}{c_0} \le \frac{0.513 h}{c_0} \tag{17}$$

where $\alpha_{\max}$ denotes the maximum value of the Courant number, which is defined as $\alpha = c\Delta t / h$ (Sei and Symes, 1995; Dablain, 1986) where Δt and h are the temporal and the spatial step size, respectively. When the 3D PAM is used to solve the 3D anisotropic elastic wave equation, we roughly estimate the temporal increment, which should also satisfy the second inequality [eq. (17)] (Yang et al., 2003, 2012).

The dispersion rate R is defined as the ratio of the numerical phase velocity to the real phase velocity, $R = \frac{c_{num}}{c_0} = \frac{\omega_{num}\Delta t}{\alpha\theta} = \frac{\gamma}{\alpha\theta}$, while $\gamma = \omega_{num}\Delta t$, $\theta = \left|\vec{k}\right| h = 2\pi S_p$. The PAM dispersion curves for different conditions are shown in Figs. 2-5. These curves are computed using PAM for the acoustic wave equation at different propagation angles to the x-axis (δ_1) and z-axis (δ_2), changing with the spatial sampling ratio $S_p = \frac{h}{\lambda}$ (Moczo et al., 2000). $R = 1$ means the method introduces no numerical dispersion; whereas it suffers from different amount of numerical dispersions when R is different from one.

Figs. 2-5 present the dispersion relationship of the PAM with different Courant numbers ($\alpha = 0.1, 0.3, 05$) and different δ_2 but the same $\delta_1 = 0^{\circ}$. The results show that the numerical dispersion increases with the Courant number and the spatial step. The maximal dispersion error of the PAM for all cases is less than 3.1%, whereas that of the LWC and SG methods is 23% and 24%, respectively. Furthermore, the anisotropic characteristics is also revealed. Regardless, there is a difference of less than 1% in the R between different propagation directions and Courant numbers for the PAM. This result demonstrates that the numerical dispersion is not sensitive to the Courant number and propagation direction and that the PAM has less numerical dispersion and less numerical dispersion anisotropy than the other methods. The maximum numerical dispersion error and numerical dispersion anisotropic error of the different methods are listed in Table 1. The results highlight the advantages of the PAM for suppressing the numerical dispersion over the traditional LWC and SG methods.
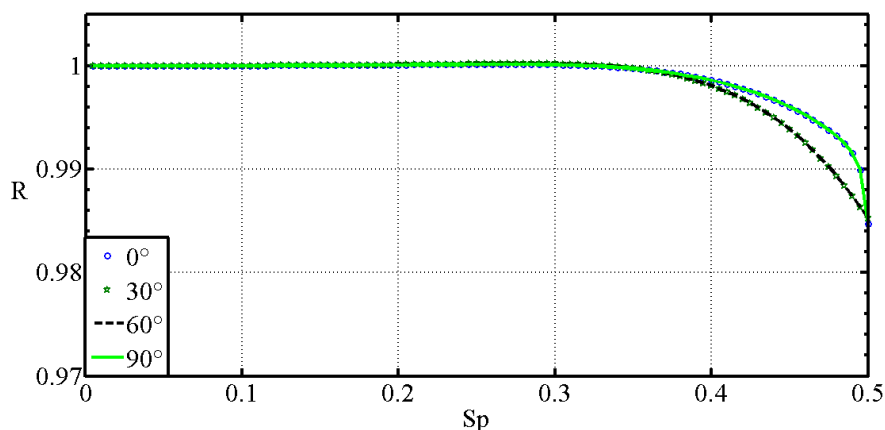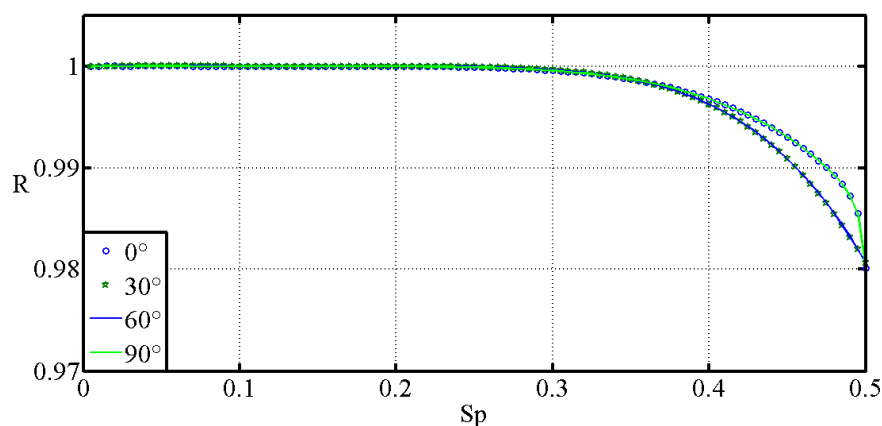
Fig. 2. The ratio R of the numerical velocity (c_{num}) to the exact phase velocity (c_0) versus the spatial sampling ratio Sp generated by the PAM for the Courant number α=0.2 and different wave propagation angles; the angle with the x-axis (δ_1) δ_1=0° is fixed, and the angles with the z-axis (δ_2) δ_2 are 0°, 30°, 60°, and 90°, respectively.

Fig. 3. The ratio R of the numerical velocity (c_{num}) to the exact phase velocity (c_0) versus the spatial sampling ratio Sp generated by the PAM for the Courant number α=0.3 and different wave propagation angles; the angle with the x-axis (δ_1) δ_1=30° is fixed, and the angles with the z-axis (δ_2) δ_2 are 0°, 30°, 60°, and 90°, respectively.
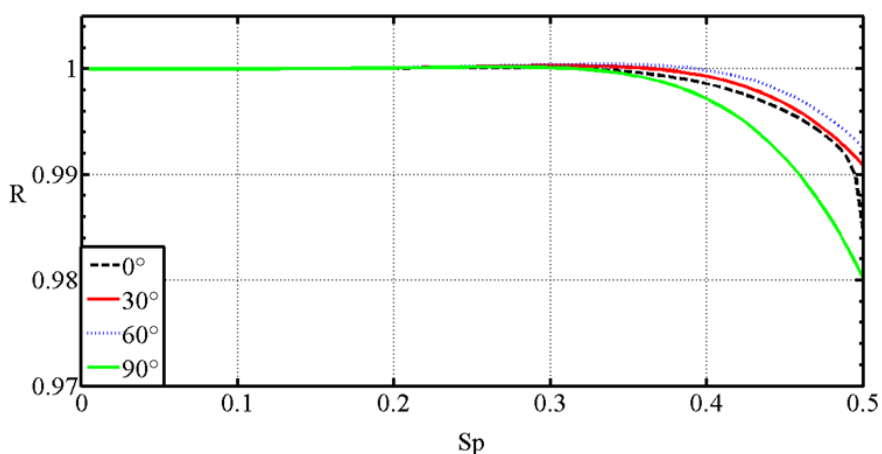

Fig. 4. The ratio R of the numerical velocity (c_{num}) to the exact phase velocity (c_0) versus the spatial sampling ratio Sp generated by the PAM for the Courant number α=0.4 and different wave propagation angles; the angle with the x-axis (δ_1) δ_1=60° is fixed, and the angles with the z-axis (δ_2) δ_2 are 0°, 30°, 60°, and 90°, respectively.
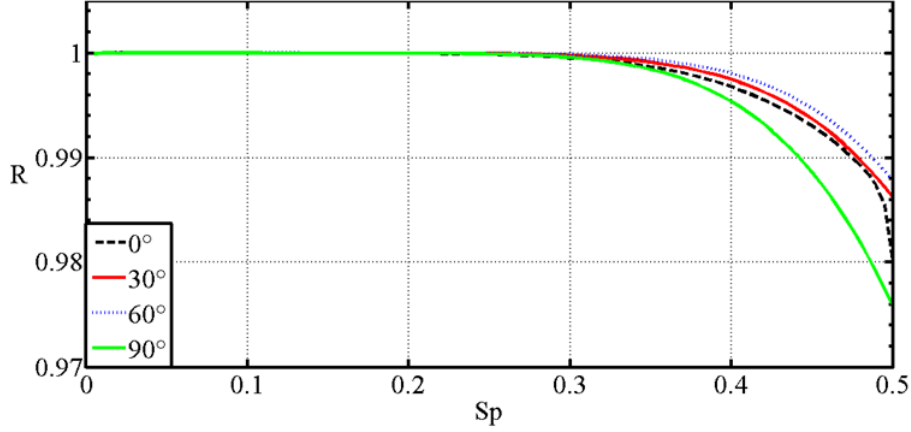
Fig. 5. The ratio R of the numerical velocity (c_{num}) to the exact phase velocity (c_0) versus the spatial sampling ratio Sp generated by the PAM for the Courant number α=0.45 and different wave propagation angles; the angle with the x-axis (δ_1) δ_1=80° is fixed, and the angles with the z-axis (δ_2) δ_2 are 0°, 30°, 60°, and 90°, respectively.

Table 1. The maximum numerical dispersion error and numerical dispersion anisotropic error for different methods.

Method	The maximum numerical dispersion error （%）	Numerical dispersion anisotropic error （%）
LWC	15.6	10.1
SG	13.8	9.2
PAM	3.1	1.1

COMPUTATIONAL EFFICIENCY

In this section, we investigate the computational efficiency of the PAM for wavefield modeling, using the 3D acoustic model and homogeneous isotropic media as examples. We compare the PAM with the eighth-order LWC method (Dablain, 1986) and the eighth-order SG method (Virieux, 1986) to demonstrate the higher computational efficiency of PAM. All numerical experiments were performed on a workstation with an Intel(R) Xeon(R) CPU with 2.60 GHz and 64 GB memory.

In the following experiment, the force source $f(t)$ located at the center of the model is a Ricker wavelet with the following expression：

$$f(t) = -5.76f_0^2[1-16\left(0.6f_0t-1\right)^2]\exp[-8\left(0.6f_0t-1\right)^2], \tag{18}$$

where f_0 is approximately twice the peak value of the amplitude spectrum. It approximates the maximum frequency of the signal $f(t)$ and thus provides the minimum wavelength in the wavefield. In our program, the source function is added to the displacement u_1, and in the elastic case, it will excite both the P- and S-waves.

We use $f_0 = 25\,\text{Hz}$, the computational domain is $0 < x, y, z \le 5.5\ \text{km}$, and the constant acoustic velocity $c = 4000$ m/s. The time and spatial increments are $\Delta t = 0.0025$ s and $h = \Delta x = \Delta y = \Delta z = 55$ m, respectively, resulting in a number of sampling points per wavelength of $G = \dfrac{4000}{25 \times 55} \approx 2.90$, which is less than 3.

Fig. 6 shows the wavefield snapshots in the x-y plane at $\mathrm{T} = 0.66$ s for the same computational parameters for (a) the PAM, (b) the eighth-order LWC method, and (c) the eighth-order SG method. The wavefronts of the seismic waves generated by the three methods are identical. However, the snapshots in Figs. 6(b) and 6(c) for the eighth-order LWC and SG methods show strong numerical dispersion and numerical dispersion anisotropy, whereas the PAM [Fig. 6(a)] exhibits no visible numerical dispersion.
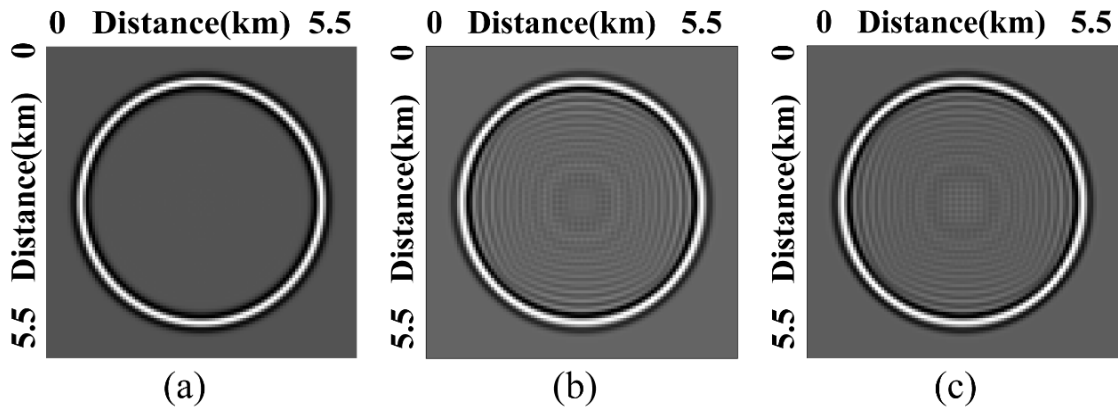

Fig. 6. Wavefield snapshots in the x-y plane at $\mathrm{T} = 0.6$ s with the computational parameters $\Delta t = 0.0025$ s, $h = \Delta x = \Delta y = \Delta z = 55$ m, $f_0 = 25\,\text{Hz}$ computed by (a) the PAM, (b) the eighth-order LWC, and (c) the eighth-order SG method.

We increase the number of spatial sampling grid points per wavelength for the same Courant number for the LWC and SG method to eliminate the numerical dispersion; the time step is also reduced proportionally. We repeat the wavefield simulation until there is no more visible numerical dispersion. In this case, the numerical simulation results show that the fine-grid step increment of the LWC is $\Delta x = \Delta y = \Delta z = 25$ m, and that of the eighth-order SG is $\Delta x = \Delta y = \Delta z = 28$ m. The results indicate that the PAM provides the same result for a coarse grid ($\Delta x = \Delta y = \Delta z = 55$ m) as that of the

LWC and SG methods for finer grids $\Delta x = \Delta y = \Delta z = 25$ m and $\Delta x = \Delta y = \Delta z = 28$ m. For the same computational region and the same Courant number, it took the PAM 27.5 s, the eighth-order LWC 124.5 s, and the SG 87.4 s to obtain the same numerical result with no dispersion. This result implies that the computational speed of the PAM is 4.53 times that of the eighth-order LWC and 3.18 times that of the eighth-order SG to achieve the same accuracy. Regarding the storage costs, the numbers of grid points of the eighth-order LWC and SG methods are $221 \times 221 \times 221$ and $197 \times 197 \times 197$, respectively, whereas that of the PAM is only $101 \times 101 \times 101$ for the coarse grid (h = 55 m) for the same computational domain. This result indicates that the memory requirement of the PAM is approximately 23.8% that of the eighth-order LWC method and approximately 33.67% that of the eighth-order SG scheme. Table 2 lists the details of the computational costs of the three eighth-order methods to generate an output without visible numerical dispersion in the same computational region and for the same Courant number. The results demonstrate that the PAM has significantly lower computer memory requirements and higher computational efficiency than the traditional eighth-order LWC and SG methods.

Table 2. Comparison of the CPU time costs and the memory requirements of the eighth-order LWC, SG, and PAM to produce a result without numerical dispersion.

Methods	h (km)	mesh points	CPU time		Memory Requirement(%)
			(s)	(%)	
eighth-order LWC	25	$221 \times 221 \times 221$	87.4	318	419
eighth-order SG	28	$197 \times 197 \times 197$	124.5	453	297
PAM	55	$101 \times 101 \times 101$	27.5	100	100

We conduct a comparison of the waveforms computed from the different methods to understand the numerical dispersion property of PAM. We double the computational domain of the space and time range while keeping the other parameters the same. The receiver located at $R(7.7 \text{ km}, 5.5 \text{ km}, 5.5 \text{ km})$ is selected to record the waveforms generated by the three methods. Fig. 7 shows the waveforms recorded at the receiver in a coarse grid ($\Delta x = \Delta y = \Delta z = 55$ m), where the dashed lines denote the exact solution calculated using the Cagniard-de Hoop method (de Hoop, 1960), and the solid lines denote the numerical solutions calculated with the three eighth-order methods (PAM, LWC, and SG). Fig. 7 (a) shows that the waveform computed by the PAM is consistent with the analytic solution, but the eighth-order LWC and SG methods exhibit strong numerical dispersions with the amplitudes oscillates from the analytical solution for the same grid size. This result demonstrates that the PAM method is capable of providing sufficiently accurate results as the analytic solution and does

not suffer from numerical dispersion caused by discretizing the wave equation for the coarse mesh. In other words, the results suggest that the PAM has higher computational efficiency and requires less memory than the other two methods if a coarse mesh is used for large-scale wavefield simulations.
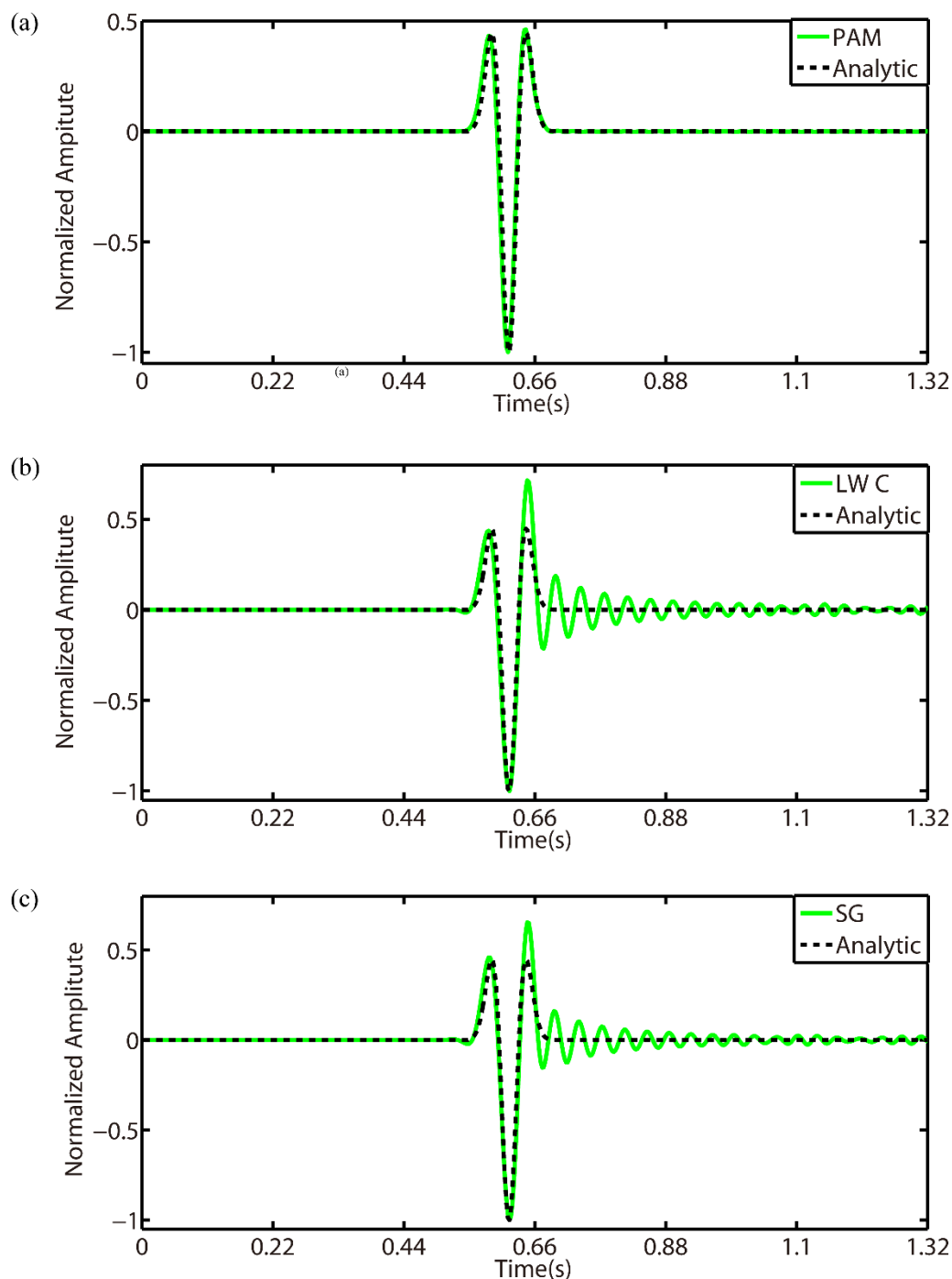

Fig. 7. Comparisons of the waveform records at the receiver $R_1(7.7\,\text{km}, 5.5\,\text{km}, 5.5\,\text{km})$ for the analytic solution (dashed line) and the numerical solution (solid line) computed by the (a) PAM, (b) LWC, and (c) SG using relatively coarse grids with the computational parameters $\Delta t = 0.0025\,\text{s}$, $h = \Delta x = \Delta y = \Delta z = 55\,\text{m}$, and $f_0 = 25\,\text{Hz}$.

3D NUMERICAL SIMULATIONS WAVE-FIELD MODELING

In this section, we describe the numerical experiments to demonstrate the effectiveness of the PAM for suppressing the numerical dispersion using different acoustic and elastic models. The results are compared with those of the eighth-order LWC method, and the eighth-order SG method.

Two-layer acoustic model

In the first experiment, we test the acoustic wave propagation in a two-layer medium with strong velocity changes. A model domain of $7\,\text{km} \times 7\,\text{km} \times 7\,\text{km}$ is chosen, with a grid number of $201 \times 201 \times 201$, and the spatial increment and temporal step are $h = \Delta x = \Delta y = \Delta z = 35$ m and $\Delta t = 0.75$ s, respectively. The two-layer acoustic model consists of a 2.0 km/s layer above a 4.0 km/s layer. The horizontal interface is at a depth of 3.5 km. The source wavelet is a symmetric Ricker wavelet with $f_0 = 20$ Hz peak frequency, which is the same expression as eq. (18). The force source is located 350 m below the regional center. These parameters result in a sampling number of grid points per minimum wavelength of G = 2.86, which is less than 3.

Fig. 8 shows the wavefield snapshots in the *x-z* and *x-y* plane at T = 1.05 s for the two-layer medium model, in which (a) and (d), (b) and (e), and (c) and (f) are computed by the PAM, LWC, and SG, respectively. The
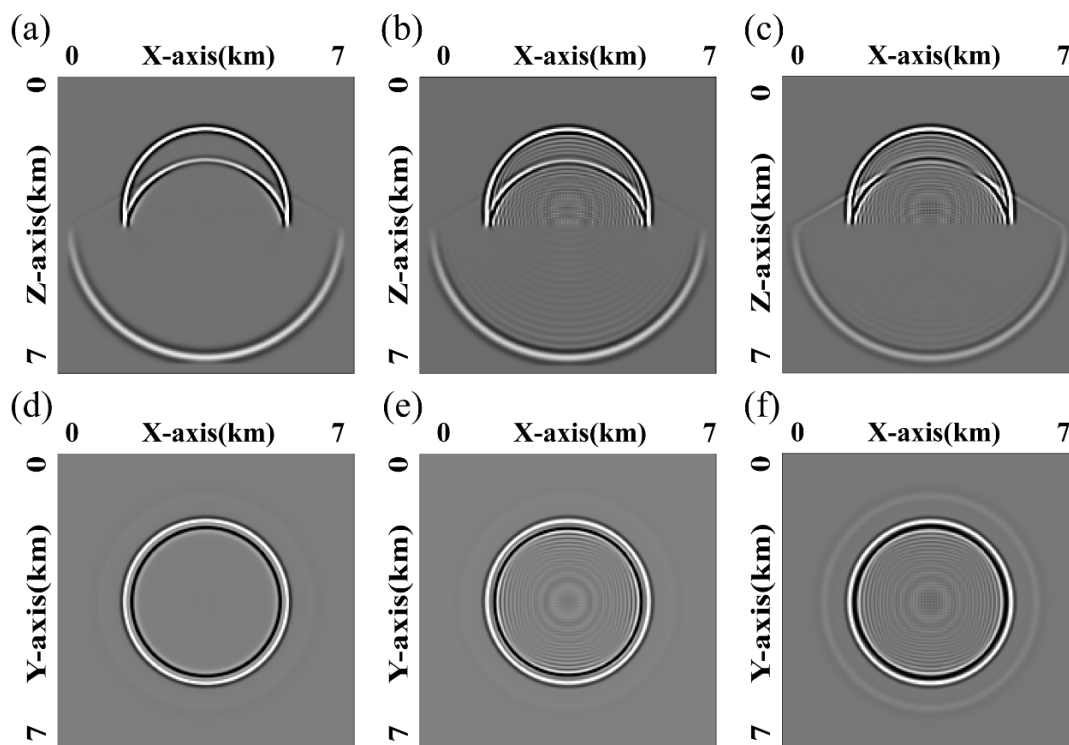

Fig. 8. The wavefield snapshots in the x-z and x-y plane at T=1.05 s for the two-layer acoustic model; (a) and (d), (b) and (e), and (c) and (f) are computed by the PAM, LWC, and SG, respectively.

snapshots in the *y-z* plane are the same as in Fig. 8 due to the symmetry. In the wavefield snapshot in Figs. 8(a) and 8(d), we can observe the direct wave, the refraction wave, and the reflection of the acoustic wave from the inner interface. The wavefield snapshot calculated by PAM has almost no numerical dispersion, even if there is a two-fold difference in the model velocity between the adjacent layers. However, the snapshots of the LWC and SG methods show strong numerical dispersions.

For the same model, much higher resolution space and time grids of $\Delta x = \Delta y = \Delta z = 10$ m and $\Delta t = 0.2$ ms are needed for the eighth-order LWC method to produce approximately equivalent results (Ma et al., 2011). Fig. 9(a) shows the comparisons of the waveforms recorded at the receiver $R(3.5 \, \text{km}, 3.5 \, \text{km}, 2.73 \, \text{km})$ computed by the PAM for the coarse grids ($\Delta x = \Delta y = \Delta z = 35$ m) and the eighth-order LWC for the fine grids ($\Delta x = \Delta y = \Delta z = 10$ m); the two waveforms in Fig. 9(b) are computed by the SG method for the coarse grids ($\Delta x = \Delta y = \Delta z = 35$ m) and the eighth-order LWC method for the fine grids ($\Delta x = \Delta y = \Delta z = 10$ m). A comparison of the results indicates that the PAM method can provide an equivalent solution for much coarser grids for the two-layer model with a strong interface while requiring much less computation time and computer memory than the other methods.
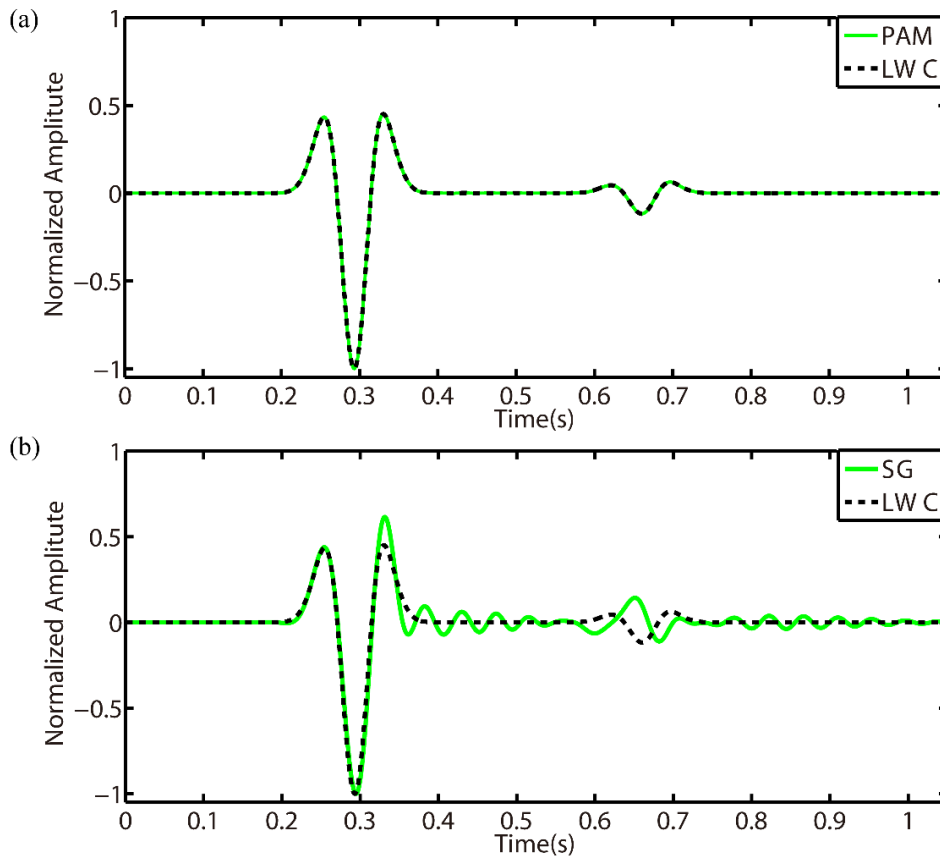

Fig. 9. The comparison of the waveforms records at receiver $R(3.5 \, \text{km}, 3.5 \, \text{km}, 2.73 \, \text{km})$ for the eighth-order LWC using fine grids (dashed lines) and the numerical solution using coarse grids (solid lines) generated by the PAM and SG methods for the two-layer acoustic model.

Isotropic elastic model

We use the 3D isotropic elastic model to determine the validity of the PAM in complex cases. According to eq. (9), we rewrite the wave equation for elastic case as follows:

$$
\begin{cases}
\rho\dfrac{\partial^2 u_1}{\partial t^2} = \mu\Delta u_1 + (\lambda+\mu)\left(\dfrac{\partial^2 u_1}{\partial x^2} + \dfrac{\partial^2 u_2}{\partial x\partial y} + \dfrac{\partial^2 u_3}{\partial x\partial z}\right) + f_1(t)\delta(x-x_s, y-y_s, z-z_s)\\[2ex]
\rho\dfrac{\partial^2 u_2}{\partial t^2} = \mu\Delta u_2 + (\lambda+\mu)\left(\dfrac{\partial^2 u_1}{\partial x\partial y} + \dfrac{\partial^2 u_2}{\partial y^2} + \dfrac{\partial^2 u_3}{\partial y\partial z}\right) + f_2(t)\delta(x-x_s, y-y_s, z-z_s)\\[2ex]
\rho\dfrac{\partial^2 u_3}{\partial t^2} = \mu\Delta u_3 + (\lambda+\mu)\left(\dfrac{\partial^2 u_1}{\partial x\partial z} + \dfrac{\partial^2 u_2}{\partial y\partial z} + \dfrac{\partial^2 u_3}{\partial z^2}\right) + f_3(t)\delta(x-x_s, y-y_s, z-z_s)
\end{cases}
$$

$$(19)$$

where $u = (u_1, u_2, u_3)$. Here, we choose the elastic constants $\lambda = 4.75$ GPa, $\mu = 3.75$ GPa, and the density $\rho = 2.1$ g/cm³. The spatial and time increments are respectively $\Delta x = \Delta y = \Delta z = 20$ m and $\Delta t = 0.5\times10^{-3}$ s, and the number of grid points is $181\times181\times181$. The force source located at $(x_s, y_s, z_s) = $ (1.8 km, 1.8 km, 1.8 km) is the same as the one used in the acoustic experiments, and the peak frequency is $f_0 = 15$ Hz. The parameters corresponding to the P- and SV-wave velocity are $V_S = 1.336$ km/s and $V_P = 2.415$ km/s, respectively.
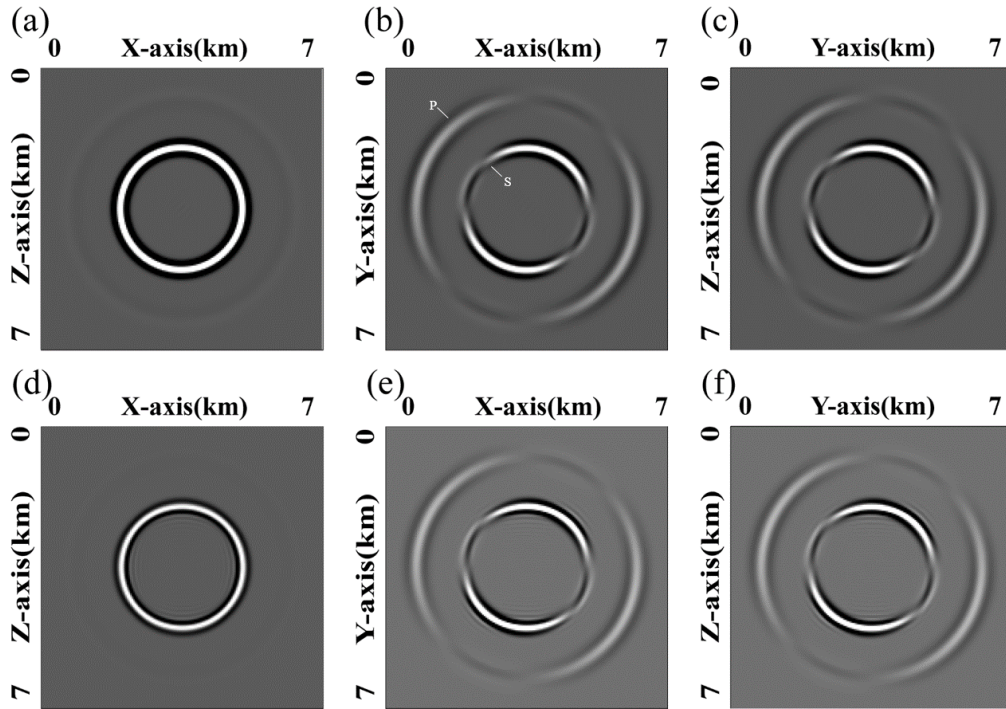

Fig. 10. The wavefield snapshots in the x-z, x-y, and y-z planes of the displacement component u_2 at T= 0.7 s for the elastic model; (a)–(c) and (d)–(f) are generated by the PAM and LWC, respectively.

Figs. 10 shows the wavefield snapshots in the *x-z, x-y*, and *y-z* planes of the displacement component u_2 at T = 0.7 s for the elastic model; Figs. 10(a)–(c) and 10(d)–(f) are the results of the PAM and LWC methods, respectively. According to the properties of the homogeneous isotropic medium model, the wavefield snapshots of the other two components can be obtained due to the symmetry. The snapshots in the *x-y* and the *y-z* planes [Fig. 10(b) and 10(c)] show clear wavefronts of the P- and SV-waves. The snapshot in the *x-z* plane [Fig. 10 (a)] shows a clear wavefront of the SH-wave but a very weak wavefront of the P-wave. The wavefield snapshots generated by the PAM exhibit almost no numerical dispersion, even when the number of grid points per minimum wavelength is about 3.3. However, the snapshot generated by the LWC [Fig. 10 (d)-(e)] shows wave scattering and numerical anisotropy. Fig. 11 shows the comparison of the waveforms recorded at receiver R (0.3 km, 0.3 km, 0.3 km) from 0 to 0.7 s generated by the PAM method (solid line) and the analytic solution (dashed line) (Aki and Richards, 1980; Carcione, 2014). It is evident that the waveforms of the three components are all in agreement with the analytic solution. This result demonstrates the effectiveness of PAM for simulating the wavefield in a homogeneous isotropic medium.

Vertical transversely isotropic (VTI) model

In practical applications, anisotropy of the Earth's interior is commonly observed in vertically aligned media or fractures (Song et al., 2012). The investigation of the anisotropy of underground media is a challenging task in seismic exploration and oil and gas production. Therefore, numerical simulations of the seismic waves in an anisotropic medium have practical applications.

In this section, we describe the performance of the PAM method for the elastic case in anisotropic media. We consider the strong form of the seismic wave equation in a 3D vertical transversely isotropic (VTI) medium, with the symmetry axis in the *z*-direction. The VTI elastic wave equations are defined as follows:

$$\begin{cases} \rho \dfrac{\partial^2 u_1}{\partial t^2} = c_{11} \dfrac{\partial^2 u_1}{\partial x^2} + c_{66} \dfrac{\partial^2 u_1}{\partial y^2} + c_{44} \dfrac{\partial^2 u_1}{\partial z^2} + (c_{12} + c_{66}) \dfrac{\partial^2 u_2}{\partial x \partial y} + (c_{13} + c_{44}) \dfrac{\partial^2 u_3}{\partial x \partial z} + f_1(t)\delta(\mathbf{x} - \mathbf{x}_s) \\[2mm] \rho \dfrac{\partial^2 u_2}{\partial t^2} = (c_{12} + c_{66}) \dfrac{\partial^2 u_1}{\partial x \partial y} + c_{66} \dfrac{\partial^2 u_2}{\partial x^2} + c_{11} \dfrac{\partial^2 u_2}{\partial y^2} + c_{44} \dfrac{\partial^2 u_2}{\partial z^2} + (c_{13} + c_{44}) \dfrac{\partial^2 u_3}{\partial y \partial z} + f_2(t)\delta(\mathbf{x} - \mathbf{x}_s) \\[2mm] \rho \dfrac{\partial^2 u_3}{\partial t^2} = (c_{13} + c_{44}) \dfrac{\partial^2 u_1}{\partial x \partial z} + (c_{13} + c_{44}) \dfrac{\partial^2 u_2}{\partial y \partial z} + c_{44} \dfrac{\partial^2 u_3}{\partial x^2} + c_{44} \dfrac{\partial^2 u_3}{\partial y^2} + c_{33} \dfrac{\partial^2 u_3}{\partial z^2} + f_3(t)\delta(\mathbf{x} - \mathbf{x}_s) \end{cases}$$
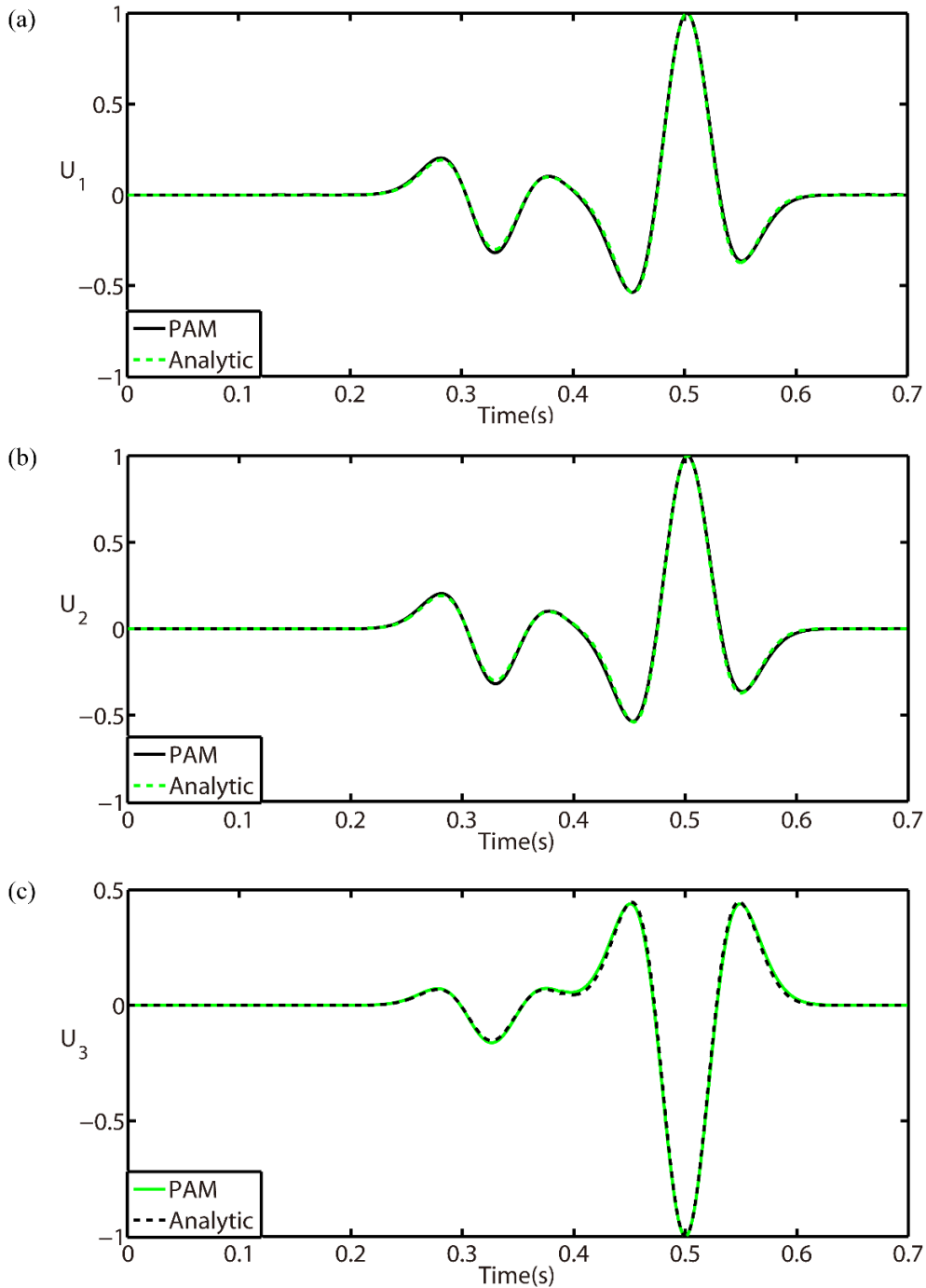
(20)

Fig. 11. The comparison of the waveforms recorded at receiver R (0.3 km, 0.3 km, 0.3 km) from 0 to 0.7 s for the elastic model generated by the PAM (solid line) and the analytic solution (dashed line); (a), (b), and (c) are the waveforms for the components u_1, u_2, and u_3, respectively.

For this numerical experiment, the computational domain is $0 < x, y, z \leq 6$ km, and the source function with $f_0 = 20$ Hz is located at the center of the domain, which is the same as in the experiment of the isotropic elastic model. The computational parameters are $\Delta x = \Delta y = \Delta z = 30$ m and $\Delta t = 0.8 \times 10^{-3}$ s. The parameters of the medium are listed in Table 3. The

wavefield snapshots of the three components of displacement (u_1, u_2, and u_3) at time T = 0.88 s in the *x-y, x-z,* and *y-z* planes are shown in Fig. 12. The wavefront of the quasi-P (qP) waves and quasi-S waves in the *x-y* plane are perfect circles, indicating isotropy in the *x-y* plane for the wave propagation. Whereas the other snapshots in Fig. 12 show that the wavefronts of the qP waves, quasi-SV (qSV) waves, and quasi-SH (qSH) waves are elliptical, indicating that the propagation velocities of these waves are directional dependent. The qSV wavefronts have cusps and triplications, depending on the value of c_{13} (Faria and Stoffa, 1994). Triplications can be observed in the horizontal component qSV wavefronts in the *x-z* plane for the u_1 component [Fig. 12(d)], the *y-z* plane for the u_2 component [Fig.12(h)], and the vertical component qSV wavefronts [Fig. 12(f) and 12(i)]. S-wave splitting (Bansal and Sen, 2008; Yang and Wang, 2010) is evident in the wavefield snapshots of the *x-* and *y-*components on the *x-z* and *y-z* planes, respectively.
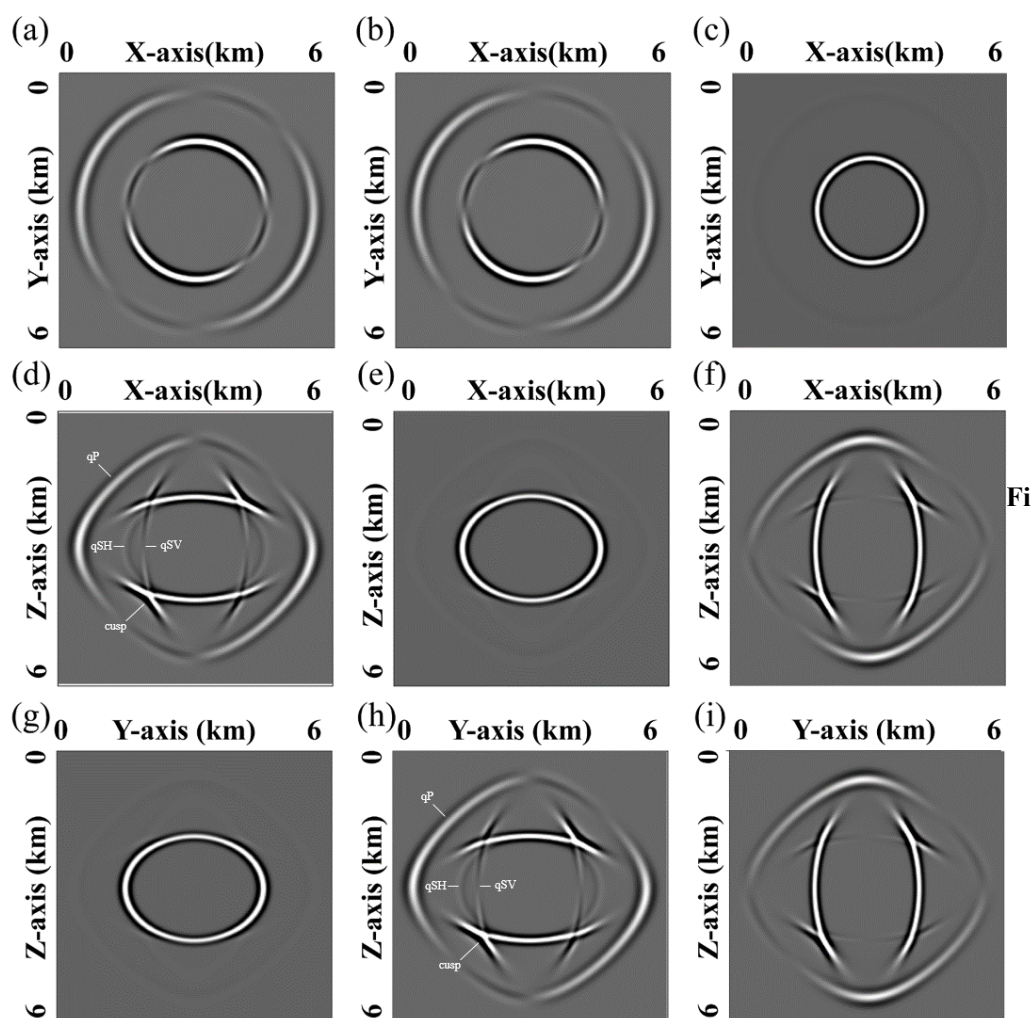

Fig. 12. Snapshots of the three components of the displacement in the vertical transversely isotropic medium at T=0.88 s generated by the PAM; (a)–(c), (d)–(f), and (g)–(i) are the snapshots for the u_1, u_2, and u_3 components, in the x-y, x-z, and y-z planes, respectively.

Table 3. Medium parameters used in the VTI model.

c_{11} (GPa)	c_{12} (GPa)	c_{13} (GPa)	c_{33} (GPa)	c_{44} (GPa)	c_{66} (GPa)	ρ_s (g/cm^3)
20	6	4.5	17.5	4	7	1.8

DISCUSSIONS and CONCLUSIONS

In this study, the PAM scheme was developed for 3D seismic modeling and used the SMM operators (Tong et al., 2013) for spatial discretization and the Padé approximation for time-marching. This proposed method had fourth-order accuracy in time and eighth-order accuracy in space. The theoretical analysis of PAM, including the stability conditions and numerical dispersion relations in the 3D, were presented. The results showed that the high-order PAM has stricter stability criterion but higher accuracy in the numerical simulations and the smallest numerical dispersion error compared to the traditional finite difference methods, such as the LWC and SG. We applied the PAM to simulate the acoustic and elastic wave propagation in different 3D medium models, including a two-layer acoustic model, an isotropic elastic model, and a VTI model. We also compared the computational efficiencies and the numerical modeling results of the PAM with those of the eighth-order LWC method and the SG method. The acoustic wave propagation in the two-layer model (Figs. 8-9) and the elastic wavefield snapshots (Figs. 10-11) showed that the PAM provided accurate results for the layered models without any special treatment at the interfaces. The elastic wave simulation of the VTI model (Fig. 12) showed that the PAM could precisely model the cusps, triplications, and the S-wave splitting in the wavefield. All experiments were performed on relatively coarse grids, and the results demonstrated that the PAM exhibited low numerical dispersion and high computational efficiency.

The theoretical analysis and the numerical simulations indicated the following numerical advantages of the PAM:

1. For the spatial discretization, the wavefield gradient information was added to discretize the higher-order spatial derivatives. As a result, the wave propagation simulation contained more wavefield information, which increased the precision and imaging quality of the seismic inversion or seismic migration.

2. For the same Courant number, the PAM had the smallest numerical dispersion when compared with the traditional finite difference schemes, such as the eight-order LWC and SG methods. The PAM also exhibited good performance regarding numerical dispersion anisotropy.

3. The PAM had high numerical accuracy. The waveforms computed by the PAM were consistent with the analytic solution for the coarse grid, indicating that the PAM method provided sufficiently accurate results for the coarse mesh.

4. The PAM proved suitable for wavefield simulation for coarse spatial grids or models with strong velocity difference between adjacent layers. The method had high computational efficiency and low storage space requirements.

5. The PAM also exhibited low numerical dispersion for simulating the elastic wave equations in a complex medium.

ACKNOWLEGEMENTS

REFERENCES

Alterman, Z. and Karal, F.C., 1968. Propagation of seismic wave in layered media by finite difference method. Bull. Seismol. Soc. Am., 58: 367-398.

Abdulkadir, Y.A., 2015. Comparison of finite difference schemes for the wave equation based on dispersion. J. Appl. Mathemat. Phys., 3: 1544-1562.

Aki, K. and Richards, P.G., 1980. Quantitative Seismology: Theory and Methods. W.H. Freeman & Co., San Francisco.

Alterman, Z. and Karal F.C., 1968. Propagation of seismic wave in layered media by finite difference method. Bull. Seismol. Soc. Am., 58: 367-398.

Bansal, R. and Sen, M.K., 2008. Finite-difference modelling of s-wave splitting in anisotropic media. Geophys. Prosp., 56: 293-312.

Blanch, J.O. and Robertsson, J.O.A., 2010. A modified Lax-Wendroff correction for wave propagation in media described by Zener elements. Geophys. J. Roy. Astronom. Soc., 131: 381-386.

Booth, D.C. and Crampin, S., 2010a. The anisotropic reflectivity technique: theory. Geophys. J. Roy. Astronom. Soc., 72: 755-766.

Booth, D.C. and Crampin, S., 2010b. The anisotropic reflectivity technique: anomalous reflected arrivals from an anisotropic upper mantle. Geophys. J. Internat. 72: 767-782.

Bouchon, M., 1996. The discrete wave number formulation of boundary integral equations and boundary element methods: a review with applications to the simulation of seismic wave propagation in complex geological structures. Pure Appl. Geophys., 148: 3-20.

Carcione, J.M. and Helle, H.B., 1999. Numerical solution of the poroviscoelastic wave equationon a staggered mesh. J. Computat. Phys., 154: 520-527.

Carcione, J.M., 2014. Wave Fields in Real Media. Theory and numerical simulation of wave propagation in anisotropic, anelastic, porous and electromagnetic media, 3rd ed. Elsevier Science Publishers, Amsterdam.

Carcione, J.M., Dan, K., Behle, A. and Seriani, G., 1992. A spectral scheme for wave propagation simulation in 3-D elastic-anisotropic media. Geophysics, 57: 1593-1607.

Carcione, J.M., Herman, G.C. and ten Kroode, A.P.E., 2002. Seismic modeling. Geophysics, 67: 1304-1325.

Chen, X., 1993. A systematic and efficient method of computing normal modes for multilayered half-space. Geophys. J. Internat., 115: 391-409.

Dablain, M.A., 1986. The application of high-order differencing to the scalar wave equation. Geophysics, 51: 54-66.

Das, S., Liao, W. and Gupta, A., 2014. An efficient fourth-order low dispersive finite difference scheme for a 2-D acoustic wave equation. J. Computat. Appl. Mathemat., 258(3): 151-167.

De Hoop, A.T., 1960. A modification of Cagniard's method for solving seismic pulse problems. Appl. Sci. Res., Sect. B.8: 349-356.

Faria, E.L. and Stoffa, P.L., 1994. Finite-difference modeling in transversely isotropic media. Geophysics, 59: 282-289.

Fei, T. and Larner, K., 1995. Elimination of numerical dispersion in finite-difference modeling and migration by flux-corrected transport. Geophysics, 60: 1830-1842.

Graves, R.W., 1996. Simulating seismic wave propagation in 3D elastic media using staggered-grid finite differences. Bull. Seismol. Soc. Am., 86: 1091-1106.

Guan, Z. and Lu, J.F. 2006. Numerical Methods. Tsinghua University Press, Beijing.

He, X.J., Yang, D.H. and Wu, H., 2014. Numerical dispersion and wave-field simulation of the Runge-Kutta discontinuous Galerkin method. Chin. J. Geophys. – Chin. Ed., 57: 906-917.

He, X., Yang, D. and Wu, H., 2015. A weighted Runge-Kutta discontinuous Galerkin method for wave field modelling. Expanded Abstr., 85th Ann. Internat. SEG Mtg., New Orleans: 3349-3354.

Huang, X., Yang, D., Tong, P. and Zhou, Y., 2016. 3D nearly analytic central difference method for computation of sensitivity kernels of wave-equation-based seismic tomography. Bull. Seismol. Soc. Am., 106: 2877-2899.

Huang, X. and Sloan, D.M., 1992. The pseudospectral method for third-order differential equations. SIAM J. Numer. Analys., 29: 1626-1647.

Johnson, E.C., 1991. Adaptive finite element methods for parabolic problems, I: A linear model problem. SIAM J. Numer. Analys., 28: 43-77.

Käser, M. and Dumbser, M., 2006. An arbitrary high-order discontinuous Galerkin method for elastic waves on unstructured meshes - I. The two-dimensional isotropic case with external source terms. Geophys. J. Internat., 166: 855-877.

Komatitsch, D. and Vilotte, J.P., 1998. The spectral element method: an efficient tool to simulate the seismic response of 2D and 3D geological structures. Bull. Seismol. Soc. Am., 88: 368-392.

Kondoh, Y., Hosaka, Y. and Ishii, K., 1994. Kernel optimum nearly-analytical discretization (KOND) algorithm applied to parabolic and hyperbolic equations. Comput. Mathemat. Applicat., 27(3): 59-90.

Kosloff, D., 1984. Elastic wave calculation by the Fourier method. Bull. Seismol. Soc. Am., 74: 875-891.

Kosloff, D. , Pestana, R.C. and Tal-Ezer, H., 2010. Acoustic and elastic numerical wave simulations by recursive spatial derivative operators. Geophysics, 75(6): T167-T174.

Ma, X., Yang, D. and Liu, F., 2011. A nearly analytic symplectically partitioned Runge-Kutta method for 2-D seismic wave equations. Geophys. J. Internat., 187: 480-496.

Ma, X., Yang, D., Song, G. and Wang, M., 2014. A low-dispersive symplectic partitioned Runge-Kutta method for solving seismic-wave equations, I: Scheme and theoretical analysis. Bull. Seismol. Soc. Am., 104: 2206-2225.

Ma, X., Yang, D. and Song, G., 2015. A low-dispersive symplectic partitioned runge-kutta method for solving seismic-wave equations, II: Wavefield simulations. Bull. Seismol. Soc. Am., 105: 657-675.

448

Moczo, P., Kristek, J. and Halada, L., 2000. 3D fourth-order staggered-grid finite-difference schemes: stability and grid dispersion. Bull. Seismol. Soc. Am., 90: 587-603.

Moczo, P., Kristek, J., Vavrvčuk, V., Archuleta, R.J. and Halada, L., 2002. 3D heterogeneous staggered-grid finite-difference modeling of seismic motion with volume harmonic and arithmetic averaging of elastic moduli and densities. Bull. Seismol. Soc. Am., 92: 3042-3066.

Zhang, O.H., Liao, C., Sheng, N. and Chen, L.L., 2015. Study of Padé two-way parabolic equation and application in indoor radio wave propagation problems. Acta Electron. Sin., 8: 30.

Richtmyer, R.D. and Morton K.W., 1968. Difference methods for initial-value problems. Mathemat. Comput., 22: 465.

Salcedo, M., Novais, A., Schleicher, J. and Costa, J.C., 2017. Optimization of the parameters in complex Padé Fourier finite-difference migration. Geophysics, 82(3): S259-S269.

Sei, A. and Symes, W.W., 1995. Dispersion analysis of numerical wave propagation and its computational consequences. J. Sci. Comput., 10: 1-27.

Seriani, G., 1992. High-order spectral element method for elastic wave modeling. Expanded Abstr. 62nd Ann. Internat. SEG Mtg., New Orleans: 1285-1288.

Sidler, R. and Carcione, J.M., 2007. Wave reflection at an anelastic transversely isotropic ocean bottom. Geophysics.72(5): SM139-SM146.

Song, G.J., Yang, D.H., Tong, P. and Lian, Y.S., 2012. Parallel WNAD algorithm for solving 3D elastic equation and its wavefield simulations in TI media. Chin. J. Geophys. 55: 547-559.

Takeuchi, N. and Geller, R.J., 2000. Optimally accurate second order time-domain finite difference scheme for computing synthetic seismograms in 2-D and 3-D media. Phys. Earth Planet. Inter., 119: 99-131.

Tong, P., Yang, D., Hua, B. and Wang, M., 2013. A high-order stereo-modeling method for solving wave equations. Bull. Seismol. Soc. Am., 103: 811-833.

Vichnevetsky, R., 1979. Stability charts in the numerical approximation of partial differential equations: a review. Mathemat. Comput. Simulat., 21: 170-177.

Virieux, J., 1984. Wave propagation in heterogeneous media: velocity-stress finite-difference method. Geophysics, 49: 1933-1957.

Virieux, J., 1986. P-SV wave propagation in heterogeneous media: velocity-stress finite-difference method. Geophysics. 51: 889-901.

Wang, N. and Zhou, Y., 2014. A weak dispersion 3D wave field simulation method: a predictor-corrector method of the implicit Runge-Kutta scheme. J. Seismic Explor., 23: 431-462.

Yang, D.H., Wang, N. and Liu, E., 2012. A strong stability-preserving predictor-corrector method for the simulation of elastic wave propagation in anisotropic media. Communic. Computat. Phys., 12: 1006-1032.

Yang, L. and Sen, M.K., 2010. Finite-difference modeling with adaptive variable-length spatial operators. Geophysics, 76(4): T79-T89.

Yang, D.H., 2002. Finite element method of the elastic wave equation and wave-fields simulation in two-phase anisotropic media. Chin. J. Geophys., 45: 600-610.

Yang, D.H., Liu, E., Zhang, Z.J. and Teng, J., 2002. Finite-difference modelling in two-dimensional anisotropic media using a flux-corrected transport technique. Geophys. J. Internat., 148: 320-328.

Yang, D. and Wang, L., 2010. A split-step algorithm for effectively suppressing the numerical dispersion for 3D seismic propagation modeling. Bull. Seismol. Soc. Am., 4: 1470-1484.

Yang, D., He, X., Ma, X., Zhou, Y. and Li, J., 2016. An optimal nearly analytic discrete-weighted runge-kutta discontinuous galerkin hybrid method for acoustic wavefield modeling. Geophysics, 81(5): T251-T263.

Yang, D., Song, G. and Lu, M., 2007. Optimally accurate nearly analytic discrete scheme for wave-field simulation in 3D anisotropic media. (5), 1557-1569.

Yang, D., Teng, J., Zhang, Z. and Liu, E., 2003. A nearly analytic discrete method for acoustic and elastic wave equations in anisotropic media . Bull. Seismol. Soc. Am., 93: 882-890.

Yang, D., Wang, L. and Deng, X., 2010. An explicit split‐step algorithm of the implicit adams method for solving 2-D acoustic and elastic wave equations. Geophys. J. Internat., 180: 291-310.

Yang, D., Wang, M. and Ma, X. (2014). Symplectic stereomodelling method for solving elastic wave equations in porous media. Geophys. J. Internat., 196: 560-579.

Zhou, H. and Chen, X., 2008. The localized boundary integral equation-discrete wavenumber method for simulating P-SV wave scattering by an irregular topography. Bull. Seismol. Soc. Am., 98: 265-279.

Zhou, Y., Yang, D., Ma, X. and Li, J., 2015. An effective method to suppress numerical dispersion in 2D acoustic and elastic modelling using a high-order Padé approximation. J. Geophys. Engineer., 12: 114-129.

APPENDIX A

APPROXIMATIONS OF HIGH-ORDER DERIVATIVES

We previously described the 2D equations to calculate the high-order spatial derivatives of the PAM algorithm when solving the acoustic and elastic wave equations (Zhou et al., 2015). These equations were based on the local interpolation methods in which the NAD operators were used (Konddoh et al., 1994; Yang et al., 2003; Yang et al., 2007; Yang and Wang, 2010). In this study, we extend these equations to the 3D case. When using the PAM to compute the values of U at time t_{n+1} in synthetic seismograms, high-order spatial derivatives should be computed. These equations were based on local interpolation methods that used the SMM operators. For the fourth- and fifth-order mixed partial differential operators, we used the operator-splitting method (Yang et al., 2003). The equations used in this study are as follows:

$$\frac{\partial^2 u_{i,j,k}}{\partial x^2} = \frac{1}{\Delta x^2}\left[\frac{7}{54}\left(u_{i-2,j,k}+u_{j+2,j,k}\right)+\frac{64}{27}\left(u_{i-1,j,k}+u_{i+1,j,k}\right)-5u_{i,j,k}\right]$$
$$+\frac{1}{\Delta x}\left[\frac{1}{36}\left(\frac{\partial u_{i-2,j,k}}{\partial x}-\frac{\partial u_{i+2,j,k}}{\partial x}\right)+\frac{8}{9}\left(\frac{\partial u_{i-1,j,k}}{\partial x}-\frac{\partial u_{i+1,j,k}}{\partial x}\right)\right] \tag{A-1}$$

$$\frac{\partial^3 u_{i,j,k}}{\partial x^3} = \frac{1}{\Delta x^3}\left[-\frac{31}{144}\left(u_{i-2,j,k}-u_{j+2,k}\right)-\frac{88}{9}\left(u_{i-1,j,k}-u_{j+1,j,k}\right)\right]$$
$$+\frac{1}{\Delta x^2}\left[-\frac{1}{24}\left(\frac{\partial u_{i-2,j,k}}{\partial x}+\frac{\partial u_{i+2,j,k}}{\partial x}\right)-\frac{8}{3}\left(\frac{\partial u_{i-1,j,k}}{\partial x}-\frac{\partial u_{i+1,j,k}}{\partial x}\right)-15\frac{\partial u_{i,j,k}}{\partial x}\right] \tag{A-2}$$

$$\frac{\partial^3 u_{i,j,k}}{\partial x^2 \partial z} = \frac{31}{864\Delta x^2 \Delta z}\left(u_{i+2,j,k+2} - u_{i-2,j,k-2} + u_{i-2,jk+2} - u_{i+2,j,k-2} + 2u_{i,j,k-2} - 2u_{i,j,k+2}\right)$$

$$+ \frac{44}{27\Delta x^2 \Delta z}\left(u_{i+1,j,k+1} - u_{i-1,j,k-1} + u_{i-1,j,k+1} - u_{i+1,j,k-1} + 2u_{i,j,k-1} - 2u_{i,j,k+1}\right)$$

$$- \frac{1}{144\Delta x^2}\left(\frac{\partial u_{i-2,jk-2}}{\partial z} + \frac{\partial u_{i+2,j,k+2}}{\partial z} + \frac{\partial u_{i-2,j,k+2}}{\partial z} + \frac{\partial u_{i+2,j,k-2}}{\partial z} - 2\frac{\partial u_{i,j,k+2}}{\partial z} - 2\frac{\partial u_{i,j,k-2}}{\partial z}\right)$$

$$- \frac{4}{9\Delta x^2}\left(\frac{\partial u_{i-1,j,k-1}}{\partial z} + \frac{\partial u_{i+1,j,k+1}}{\partial z} + \frac{\partial u_{i,j-1,k+1}}{\partial z} + \frac{\partial u_{i,j+1,k-1}}{\partial z} - 2\frac{\partial u_{i,j,k+1}}{\partial z} - 2\frac{\partial u_{i,j,k-1}}{\partial z}\right)$$

$$- \frac{1}{144\Delta x \Delta z}\left(\frac{\partial u_{i-2,j,k-2}}{\partial x} + \frac{\partial u_{i+2,j,k+2}}{\partial x} - \frac{\partial u_{i-2,j,k+2}}{\partial x} - \frac{\partial u_{i+2,j,k-2}}{\partial x}\right)$$

$$- \frac{4}{9\Delta x \Delta z}\left(\frac{\partial u_{i-1,j,k-1}}{\partial x} + \frac{\partial u_{i+1,j,k+1}}{\partial x} - \frac{\partial u_{i-1,j,k+1}}{\partial x} - \frac{\partial u_{i+1,j,k-1}}{\partial x}\right)$$

$$(A\text{-}3)$$

$$\frac{\partial^2 u_{i,j,k}}{\partial x \partial z} = \frac{7}{216\Delta x \Delta z}\left(u_{i-2,j,k-2} + u_{i+2,j,k+2} - u_{i-2,j,k+2}u_{i+2,j,k-2} - u_{i-2,j,k-2}\right)$$

$$+ \frac{16}{27\Delta x \Delta z}\left(u_{i+1,j,k+1} + u_{i-1,j,k-1} - u_{i+1,j,k-1} - u_{i-1,j,k+1}\right)$$

$$+ \frac{1}{144\Delta x}\left(\frac{\partial u_{i-2,jk-2}}{\partial z} - \frac{\partial u_{i+2,j,k+2}}{\partial z} + \frac{\partial u_{i-2,j,k+2}}{\partial z} - \frac{\partial u_{i+2,j,k-2}}{\partial z}\right)$$

$$+ \frac{1}{144\Delta z}\left(\frac{\partial u_{i-2,j,k-2}}{\partial x} - \frac{\partial u_{i+2,j,k+2}}{\partial x} + \frac{\partial u_{i+2,j,k-2}}{\partial x} - \frac{\partial u_{i-2,j,k+2}}{\partial x}\right)$$

$$+ \frac{4}{9\Delta x}\left(\frac{\partial u_{i-1,j,k-1}}{\partial z} - \frac{\partial u_{i+1,j,k+1}}{\partial z} + \frac{\partial u_{i-1,j,k+1}}{\partial z} - \frac{\partial u_{i+1,j,k-1}}{\partial z}\right)$$

$$+ \frac{4}{9\Delta z}\left(\frac{\partial u_{i-1,j,k-1}}{\partial x} - \frac{\partial u_{i+1,j,k+1}}{\partial x} + \frac{\partial u_{i+1,j,k-1}}{\partial x} - \frac{\partial u_{i-1,j,k+1}}{\partial x}\right)$$

$$(A\text{-}4)$$

$$\frac{\partial^3 u_{i,j,k}}{\partial x \partial y \partial z} = \frac{1}{3456 \Delta x \Delta y \Delta z}(-31(u_{i-2,j-2,k-2} - u_{i-2,j-2,k+2} - u_{i-2,j+2,k-2} + u_{i-2,j+2,k+2} - u_{i+2,j-2,k-2}$$

$$+ u_{i+2,j-2,k-2} + u_{i+2,j+2,k-2} - u_{i+2,j+2,k+2}) - 1408(u_{i-1,j-1,k-1} - u_{i-1,j-1,k+1} - u_{i-1,j+1,k-1}$$

$$+ u_{i-1,j+1,k+1} - u_{i+1,j-1,k-1} + u_{i+1,j-1,k+1} + u_{i+1,j+1,k-1} - u_{i+1,j+1,k+1})$$

$$- 6\Delta x(\frac{\partial u_{i-2,j-2,k-2}}{\partial x} - \frac{\partial u_{i-2,j-2,k+2}}{\partial x} - \frac{\partial u_{i-2,j+2,k-2}}{\partial x} + \frac{\partial u_{i-2,j+2,k+2}}{\partial x}$$

$$+ \frac{\partial u_{i+2,j-2,k-2}}{\partial x} - \frac{\partial u_{i+2,j-2,k+2}}{\partial x} - \frac{\partial u_{i+2,j+2,k-2}}{\partial x} + \frac{\partial u_{i+2,j+2,k+2}}{\partial x})$$

$$- 384\Delta x(\frac{\partial u_{i-1,j-1,k-1}}{\partial x} - \frac{\partial u_{i-1,j-1,k+1}}{\partial x} - \frac{\partial u_{i-1,j+1,k-1}}{\partial x} + \frac{\partial u_{i-1,j+1,k+1}}{\partial x}$$

$$+ \frac{\partial u_{i+1,j-1,k-1}}{\partial x} - \frac{\partial u_{i+1,j-1,k+1}}{\partial x} - \frac{\partial u_{i+1,j+1,k-1}}{\partial x} + \frac{\partial u_{i+1,j+1,k+1}}{\partial x})$$

$$- 6\Delta y(\frac{\partial u_{i-2,j-2,k-2}}{\partial y} - \frac{\partial u_{i-2,j-2,k+2}}{\partial y} + \frac{\partial u_{i-2,j+2,k-2}}{\partial y} - \frac{\partial u_{i-2,j+2,k+2}}{\partial y}$$

$$- \frac{\partial u_{i+2,j-2,k-2}}{\partial y} + \frac{\partial u_{i+2,j-2,k+2}}{\partial y} - \frac{\partial u_{i+2,j+2,k-2}}{\partial y} + \frac{\partial u_{i+2,j+2,k+2}}{\partial y})$$ (A-5)

$$- 384\Delta y(\frac{\partial u_{i-1,j-1,k-1}}{\partial y} - \frac{\partial u_{i-1,j-1,k+1}}{\partial y} + \frac{\partial u_{i-1,j+1,k-1}}{\partial y} - \frac{\partial u_{i-1,j+1,k+1}}{\partial y}$$

$$- \frac{\partial u_{i+1,j-1,k-1}}{\partial y} + \frac{\partial u_{i+1,j-1,k+1}}{\partial y} - \frac{\partial u_{i+1,j+1,k-1}}{\partial y} + \frac{\partial u_{i+1,j+1,k+1}}{\partial y})$$

$$- 6\Delta yz(\frac{\partial u_{i-2,j-2,k-2}}{\partial z} + \frac{\partial u_{i-2,j-2,k+2}}{\partial z} - \frac{\partial u_{i-2,j+2,k-2}}{\partial z} - \frac{\partial u_{i-2,j+2,k+2}}{\partial z}$$

$$- \frac{\partial u_{i+2,j-2,k-2}}{\partial z} - \frac{\partial u_{i+2,j-2,k+2}}{\partial z} + \frac{\partial u_{i+2,j+2,k-2}}{\partial z} + \frac{\partial u_{i+2,j+2,k+2}}{\partial z})$$

$$- 384\Delta z(\frac{\partial u_{i-1,j-1,k-1}}{\partial z} + \frac{\partial u_{i-1,j-1,k+1}}{\partial z} - \frac{\partial u_{i-1,j+1,k-1}}{\partial y} - \frac{\partial u_{i-1,j+1,k+1}}{\partial y}$$

$$- \frac{\partial u_{i+1,j-1,k-1}}{\partial z} - \frac{\partial u_{i+1,j-1,k+1}}{\partial z} + \frac{\partial u_{i+1,j+1,k-1}}{\partial z} + \frac{\partial u_{i+1,j+1,k+1}}{\partial z}))$$

APPENDIX B

DERIVATION OF THE STABILITY CRITERIA

In order to derive the stability condition of 3D PAM, we consider the harmonic solution of eq. (8).

$$U_{i,j,k}^{n} = \begin{pmatrix} u_{i,j,k}^{n} \\ \left(u_{x}\right)_{i,j,k}^{n} \\ \left(u_{y}\right)_{i,j,k}^{n} \\ \left(u_{z}\right)_{i,j,k}^{n} \end{pmatrix} \exp[i(k_{1}lh + k_{2}mh + k_{3}qh)] \tag{B-1}$$

where the indices i, j, and k are the spatial coordinates, n is the n-th time step of the numerical solution, h is the spatial grid length, and Δt is the temporal increment. $\vec{k} = (k_{1}, k_{2}, k_{3})$ is the wavenumber vector, and its L^{2} norm is defined as $\left|\vec{k}\right| = \left(k_{1}^{2} + k_{2}^{2} + k_{3}^{2}\right)^{1/2}$. δ_{1} and δ_{2} are the plane-wave propagation angles with respect to the x-axis and z-axis. Thus

$$k_{1} = \left|\vec{k}\right|\sin\delta_{2}\cos\delta_{1}, \ k_{2} = \left|\vec{k}\right|\sin\delta_{2}\sin\delta_{1}, \ k_{3} = \left|\vec{k}\right|\cos\delta_{2}$$

$$(0 \le \delta_{1} < 2\pi, \ 0 \le \delta_{2} < \pi).$$

By substituting eq. (B-1) into eq. (8) and rewriting the PAM numerical algorithm for the acoustic wave equation, we obtain:

$$
\begin{pmatrix} u^{n+1} \\ u_x^{n+1} \\ u_y^{n+1} \\ u_z^{n+1} \\ u^n \\ u_x^n \\ u_y^n \\ u_z^n \end{pmatrix} = G_{8\times8} \cdot \begin{pmatrix} u^n \\ u_x^n \\ u_y^n \\ u_z^n \\ u^{n-1} \\ u_x^{n-1} \\ u_y^{n-1} \\ u_z^{n-1} \end{pmatrix} \quad , \tag{B-2}
$$

where G is the amplification matrix, which is defined as:

$$
G_{8\times8} = \begin{pmatrix} g_{4\times4} & m_{4\times4} \\ I_{4\times4} & 0 \end{pmatrix},
$$

where $I_{4\times4}$ is the fourth-order identity matrix. It is not necessary to show the other element for calculating G because of the long expression.

We use the computational software Mathematica and solve $\rho(G^* \cdot G) \le 1$ and obtain the following stability condition, in which $\Delta x = \Delta y = \Delta z = h$:

$$
\alpha = \frac{c_0 \Delta t}{h} \le \alpha_{max} \le 0.513 \quad \text{or} \quad \Delta t = \frac{\alpha h}{c_0} \le \frac{\alpha_{max} h}{c_0} \le \frac{0.513 h}{c_0} \tag{B-3}
$$

where α_{max} denotes the maximum value of the Courant number, which is defined as $\alpha = c\Delta t / h$ (Sei and Symes, 1994; Dablain, 1986); Δt is the temporal step size and h is the spatial step size.

For the heterogeneous case, we can use c_0 as the maximum wave velocity of the medium.

APPENDIX C

DISPERSION RELATIONSHIP

Substitute the harmonic solutions:

$$U_{i,j,k}^{n} = \begin{pmatrix} u_{i,j,k}^{0} \\ \left(u_{x}\right)_{i,j,k}^{0} \\ \left(u_{y}\right)_{i,j,k}^{0} \\ \left(u_{z}\right)_{i,j,k}^{0} \end{pmatrix} \exp[i(-\omega_{num}n\Delta t + k_{1}lh + k_{2}mh + k_{3}qh)] \tag{C-1}$$

into eq. (8) , we obtain the numerical dispersion relation as follows:

$$Det(e^{i\gamma}I - G) = 0, \tag{C-2}$$

where $\gamma = \omega_{num}\Delta t$, G is the same as in eq. (B-2), and I is an identity matrix. From the dispersion relation (C-2), we obtain the ratio of the numerical velocity c_{num} to the exact velocity c_{0}.

The ratio of the numerical velocity to the exact phase velocity is:

$$R = \frac{c_{num}}{c_{0}} = \frac{\gamma}{2\pi\alpha S_{p}}, \tag{C-3}$$

where γ satisfies eq. (C-2), which is a nonlinear function of α, and $S_{p} = h/\lambda$, was defined by Moczo et al. (2000). Note that R is a nonlinear function of the Courant number, the sampling ratio, and the propagation angles.